Persistent spin dynamics and absence of spin freezing in the *H*-*T* phase diagram of the two-dimensional triangular antiferromagnet YbMgGaO₄

Zhaofeng Ding,[1] Zihao Zhu,[1] Jian Zhang,[1] Cheng Tan,[1] Yanxing Yang,[1] Douglas E. MacLaughlin,[2] and Lei Shu [1,3,4,*]

[1]*State Key Laboratory of Surface Physics and Department of Physics, Fudan University, Shanghai 200433, China*
[2]*Department of Physics and Astronomy, University of California, Riverside, Riverside, California 92521, USA*
[3]*Collaborative Innovation Center of Advanced Microstructures, Nanjing University, Nanjing 210093, China*
[4]*Shanghai Research Center for Quantum Sciences, Shanghai 201315, China*

We report results of muon spin relaxation and rotation (μSR) experiments on the spin-liquid candidate YbMgGaO₄. No static magnetism $\gtrsim 0.003\mu_B$ per Yb ion, ordered or disordered, is observed down to 22 mK, a factor of 2 lower in temperature than previous measurements. Persistent (temperature-independent) spin dynamics are observed up to 0.20 K and at least 1 kOe, thus extending previous zero-field μSR results over a substantial region of the *H*-*T* phase diagram. Knight shift measurements in a 10-kOe transverse field reveal two lines with nearly equal amplitudes. Inhomogeneous muon depolarization in a longitudinal field, previously characterized by stretched-exponential relaxation due to spatial inhomogeneity, is fit equally well with two exponentials, also of equal amplitudes. We attribute these results to two interstitial muon sites in the unit cell rather than disorder or other spatial distribution. Further evidence for this attribution is found from agreement between the ratio of the two measured relaxation rates and calculated mean-square local Yb³⁺ dipolar fields at candidate muon sites. Zero-field data can be understood as a combination of two-exponential dynamic relaxation and quasistatic nuclear dipolar fields.

I. INTRODUCTION

In 1973 Anderson [1] proposed an exotic magnetic state in the two-dimensional (2D) triangular-lattice Heisenberg antiferromagnet where local spins are highly entangled with no spin freezing. A clear experimental identification of such a quantum-spin-liquid (QSL) material is much desired, for its own sake and for potential applications in quantum computation and possible relation to novel phenomena such as high-temperature superconductivity, topological order, and Mott insulators [2–6]. Many materials with geometrically frustrated lattices have been proposed as candidate spin liquids (see, e.g., [7–13]). Whether there is a QSL among these candidates remains controversial, however.

YbMgGaO₄ is a quasi-2D triangular-lattice antiferromagnet that has attracted considerable attention as a QSL candidate [13–24]. No spin ordering was observed down to 0.06 K from thermodynamic and transport measurements [13,16]. The low-temperature heat capacity exhibits a power-law temperature dependence with an exponent close to the theoretical value of 2/3 for a $U(1)$ QSL. An anisotropic spin interaction was observed and discussed as important to stabilize a possible QSL ground state [14]. Inelastic neutron scattering measurements [17,18,20,24] provided evidence for a QSL state with a spinon Fermi surface by observing continuous spin excitations. High-field time-domain terahertz spectroscopy measurements [22] characterized YbMgGaO₄ as an easy-plane XXZ antiferromagnet. Theoretical treatments predict a proposed spinon Fermi surface $U(1)$ spin liquid [25–27].

Whether or not there is a QSL state in YbMgGaO₄ is still under debate. Evidence against a QSL includes thermal conductivity measurements that did not observe the expected magnetic excitation contribution down to 0.050 K [16]. Furthermore, a frequency-dependent cusp was observed at $\sim$0.1 K in ac susceptibility measurements [23], suggesting a spin-glass-like transition, although the dc magnetization saturates at low temperatures with no evidence for spin freezing up to 10 kOe [24]. Proposed alternative ground states [28–31] involve various forms of ordered or disordered static magnetism but without definite predictions for transition temperatures.

Muon spin rotation and relaxation (μSR) [32] is a powerful technique to probe local magnetism in solids and has been widely used to study spin-liquid candidates (e.g., [7,15,33–37]). A μSR study of YbMgGaO₄ by Li *et al.* [15] showed no static or long-range magnetic order in zero field (ZF) down to 0.048 K, which was taken as evidence for a $U(1)$ QSL ground state. Below 10 K the ZF muon spin polarization $P_\mu(t)$ exhibited so-called stretched-exponential relaxation $P_\mu(t) = \exp[-(\lambda^* t)^\beta]$, where λ^* is a characteristic relaxation rate and $\beta < 1$ is the stretching exponent. Stretched exponentials are used as phenomenological models for spatially inhomogeneous distributions of relaxation rates [38]. In YbMgGaO₄ $\beta \approx 0.95$ at 10 K [15], the ZF relaxation was nearly exponential. With decreasing temperature β decreased considerably, suggesting the onset of spatial inhomogeneity. At 70 mK λ^* was continuously suppressed by an applied

*Corresponding author: leishu@fudan.edu.cn

longitudinal field (LF) up to 1.8 kOe. The field dependence of β was not reported.

This article reports μSR experiments on single-crystalline YbMgGaO$_4$ that extend the work of Li *et al.* [15]. Positive-muon (μ^+) frequency and relaxation measurements were carried out for temperatures down to 22 mK and applied fields up to 10 kOe. Fourier transforms of μSR data taken in a transverse field (TF) $H_T = 10$ kOe (Sec. III A) reveal two lines with equal amplitudes but significantly different frequency (Knight) shifts. We attribute the lines to two distinct μ^+ interstitial stopping sites near the two inequivalent oxygen ions in the YbMgGaO$_4$ unit cell, as previously suggested [15]. The corrected Knight shifts K_{corr} are nearly temperature independent below 1 K, as is the bulk susceptibility χ_{mol} at this field (Ref. [24], Supplemental Material). The ratio $K_{\text{corr}}/\chi_{\text{mol}}$ is roughly consistent with calculated Yb^{3+} dipolar fields at candidate μ^+ sites.

μ^+ spin relaxation data were taken for longitudinal fields H_L up to 8 kOe at 22 mK, 0.20 K, and 5.83 K (Sec. III B), and in ZF over the temperature range 22 mK–5.8 K (Sec. III C). In light of the TF-μSR results summarized above, the LF asymmetry spectra for $T = 22$ mK and $H_L \geqslant 25$ Oe, where the relaxation is purely dynamic [32], were fit by a sum of two exponentials (rates λ_1 and λ_2) rather than the stretched exponential used previously [15]. A sum of two exponentials and a stretched exponential are both subexponential forms (i.e., exhibiting upward curvature on a log-linear plot) and can be difficult to distinguish [38].

With equal amplitudes of the two exponentials, the observed ratio $\lambda_2/\lambda_1 = 0.03(1)$ is field independent and in rough agreement with the ratio of calculated mean-square Yb^{3+} dipolar fields. This is expected if the subexponential relaxation is due to differences in coupling fields rather than inhomogeneity in the spin dynamics. It is additional evidence for the two-site scenario.

For lower H_L the contributions of static nuclear dipolar fields must be considered (stretched-exponential fits alone mix the static and dynamic contributions). Fits of relaxation functions appropriate to this situation [32] (Sec. III B) to the data then allow determination of $\lambda_1(H_L)$ down to $H_L = 0$.

The paper is organized as follows. Section II describes the YbMgGaO$_4$ sample and its crystal structure, briefly summarizes the μSR technique, and gives details of the experiment. Results of TF, LF, and ZF experiments are reported in Sec. III and are discussed in Sec. IV. Section V summarizes our conclusions.

II. EXPERIMENT

A. Sample

Platelike high-quality single crystals of YbMgGaO$_4$ were grown by a floating-zone method and characterized as reported previously [23]. Figure 1 shows two-thirds of a hexagonal unit cell of YbMgGaO$_4$ (space group $R\bar{3}m$, No. 166) [13,14]. Mg and Ga ions are distributed randomly on the indicated sites, leading to unavoidable local disorder in the structure. There are two inequivalent oxygen locations (O1 and O2) in the unit cell. The triangular 2D Yb^{3+} layers are well separated by two Mg/Ga planes and four O1/O2
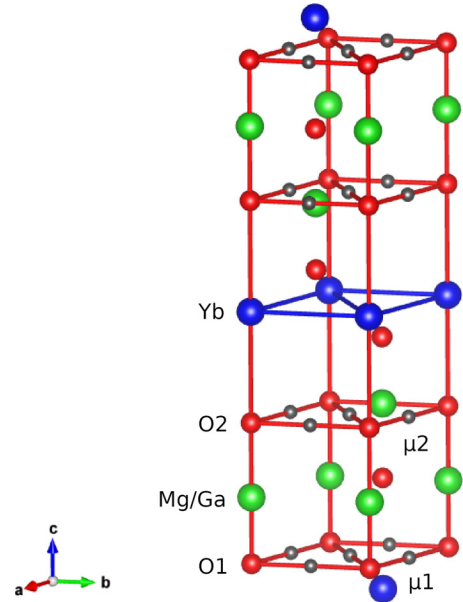

FIG. 1. Two-thirds of the unit cell of YbMgGaO$_4$ [13,14]. Blue spheres: Yb. Green spheres: Mg/Ga. Red spheres: O. Small gray spheres: candidate μ^+ sites μ1 and μ2 (see text).

planes (Yb^{3+} layer spacing 8.377 Å), and interlayer magnetic interaction is weak.

Implanted positive muons in oxides are likely to stop near O^{2-} ions. To date there are no reported calculations of μ^+ site locations in YbMgGaO$_4$ [39]. In lieu of such information, we consider candidate sites that are centered with respect to oxygen nearest neighbors. There are two such crystallographically inequivalent sites (μ1 and μ2), shown in Fig. 1. Dipolar magnetic fields from neighboring Yb^{3+} ions and nuclei are unlikely to be very different if the actual μ^+ sites are closer to O^{2-} ions.

B. The μSR technique

In a typical μSR experiment [32], $\sim$100% spin-polarized positive muons are implanted into the sample and stop at interstitial sites. Each μ^+ precesses in the (in general fluctuating) local field at its site, and at the time of its decay (mean lifetime $\sim$2.2 μs) emits a positron preferentially in the direction of the μ^+ spin. Positrons are detected by an array of scintillation counters, and a histogram $N(t)$ of count rate vs time after implantation is obtained from each counter.

For two identical counters on opposite sides of the sample, the μSR asymmetry time spectrum $A(t) = [N_1(t) - N_2(t)]/[N_1(t) + N_2(t)]$ is proportional to the component $P_\mu(t)$ of the ensemble μ^+ spin polarization $\mathbf{P}_\mu(t)$ along the axis joining the counters and the sample. Corrections for differences in counter geometries and efficiencies are straightforward [32]. Unlike its cousin NMR, which, apart from nuclear quadrupole resonance (NQR) and field-cycling techniques, requires a strong applied magnetic field to polarize the nuclear spins, the polarized μ^+ beam allows μSR to be carried out in arbitrary fields.

Experiments may be considered in three classes:

(i) In high TF-μSR, the precession frequency in a paramagnet is shifted from its value *in vacuo*. The fractional frequency

shift K (often called the Knight shift after its discoverer [40]) and its inhomogeneous distribution (often the main contribution to the linewidth) provide a microscopic characterization of the field-induced static magnetization.

(ii) In sufficiently strong LF-μSR, the resultant of applied and any local static fields is essentially parallel to the initial μ^+ spin orientation. This results in "decoupling" of the static fields, and the remaining relaxation is purely dynamic in origin [41].

(iii) In ZF- and weak LF-μSR, the time evolution of $P_\mu(t)$ is due to either or both of two mechanisms: (1) decay due to dynamic fluctuations of the local fields, and (2) μ^+ spin precession in the resultant of a distribution of (quasi) static local fields and the applied field, if any (static Kubo-Toyabe (KT) relaxation [41]). The latter are normally due to nuclear dipolar fields.

This situation can be modeled by a dynamically damped static KT function $G_{KT}(t)$:

$$P_\mu(t) = G_d(t)\, G_{KT}(t), \tag{1}$$

where the dynamic damping function $G_d(t)$ is often a simple exponential but can be more complex (as in the present work). Choices of $G_{KT}(t)$ are discussed below in Sec. III B 2. It is, however, often difficult to disentangle static and dynamic relaxation contributions from ZF-μSR data alone; this is one reason why strong LF-μSR is valuable.

C. Experimental details

A mosaic of YbMgGaO$_4$ single crystals (total mass ≈ 0.3 g) was mounted on a pure silver sample holder using diluted GE varnish, with the crystal c axes parallel to the μ^+ beam direction. μSR experiments were carried out using the dilution refrigerator spectrometer at the M15 beam line of TRIUMF, Vancouver, Canada. Field zeroing to $\lesssim 10$ mOe was achieved using a variation of the method of Morris and Heffner [42].

Data were taken over the temperature range 22 mK–8 K. Due to the large low-temperature specific heat of YbMgGaO$_4$ [16], temperatures were stabilized for 15 min before taking data. ZF- and LF-μSR data were taken with the initial μ^+ ensemble spin polarization parallel to the crystal c axes. For TF-μSR the μ^+ spins were rotated by $\sim 90°$ before implantation. Data were analyzed using the Paul Scherrer Institute MUSRFIT fitting program [43] and the TRIUMF PHYSICA programming environment [44].

III. RESULTS

A. Transverse-field μSR

TF-μSR experiments were carried out in YbMgGaO$_4$ over the temperature range 26 mK–0.825 K in a transverse applied field $H_T = 10$ kOe. Representative Fourier transforms of TF asymmetry time spectra are shown in Fig. 2. They exhibit three lines: line 1 [Fig. 2(a)], which is very broad and shifted to higher frequency, and lines 2 and 3 [Fig. 2(b)], which are narrow and overlap considerably.

The original TF asymmetry time spectra $A^{TF}(t)$ (not shown) were therefore fit by a sum of three Gaussian-damped
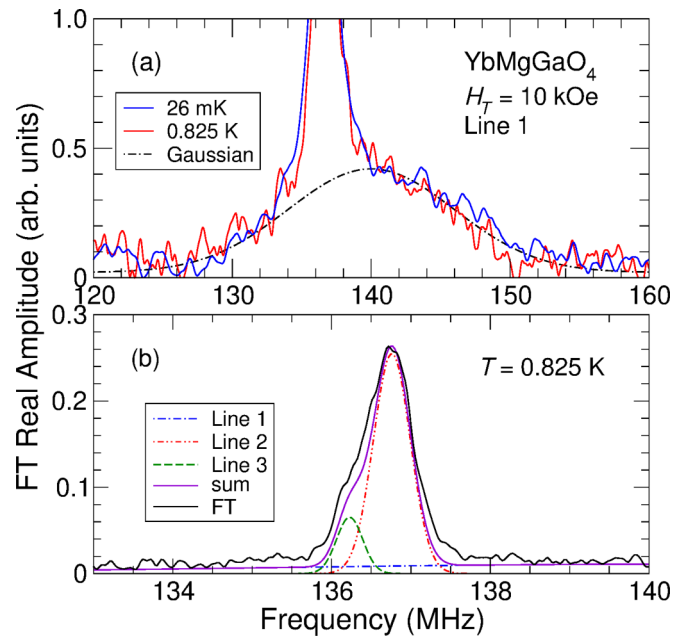

FIG. 2. Fourier-transform (FT) μ^+ spectra from YbMgGaO$_4$, $H_T = 10$ kOe. (a) Wide-frequency FTs at 26 mK (blue) and 0.825 K (red). The narrow peak is distorted (broadened) by strong apodization. (b) Narrow-frequency FT, $T = 0.825$ K. Curves: Fourier transforms of Gaussian terms 1–3 [Eq. (2)] and their sum (see text).

oscillating components:

$$A^{TF}(t) = \sum_{i=1}^{3} A_i^{TF} \exp\left(-\frac{1}{2}\sigma_i^2 t^2\right) \cos(\omega_i t + \varphi), \tag{2}$$

where a common phase φ was assumed. Parameter values for $T = 26$ mK are listed in Table I. Amplitudes A_1^{TF} and A_2^{TF} from the fits are nearly equal and considerably larger than A_3^{TF}. The curves in Fig. 2 are Fourier transforms of the Gaussian asymmetry terms in Eq. (2), with parameters from the fits: frequencies $\omega_i/2\pi$, widths $\sigma_i/2\pi$, and areas proportional to A_i. Their sum is normalized to the experimental Fourier transform in Fig. 2(b).

One of the three lines arises from muons that miss the sample and stop in the silver sample holder, and the other two are from the sample. Line 3, which is the narrowest, is assumed to be the "silver" signal, and $\omega_3/2\pi$ is used as the reference frequency for the Knight shifts of the other two components. Additional evidence for this attribution is discussed below in Sec. III B 1. The sample lines are numbered in order of their shifts (Fig. 2), consistent with the μ^+ site numbering in order of their distance from the nearest Yb^{3+} layer (Fig. 1).

In order for Knight shifts to reflect local magnetism, a correction must be made for the contributions to the raw shift K_{raw} from macroscopic Lorentz and demagnetizing fields [45]:

$$K_{corr} = K_{raw} - A_{Ld}\, \chi_{mol}, \tag{3}$$

where $A_{Ld} = 4\pi(\frac{1}{3} - D)/v_{mol}$, χ_{mol} is the molar bulk susceptibility, D is the sample demagnetization coefficient, and v_{mol} is the molar volume (50.6 cm^3/mol for YbMgGaO$_4$). For field normal to the thin mosaic samples, D is estimated to be 0.8(1),

TABLE I. Parameters A_i^{TF}, ω_i, and σ_i from fits of Eq. (2) to μ^+ asymmetry time spectra from YbMgGaO$_4$, $H_T = 10$ kOe, $T = 26$ mK. Hyperfine coupling constants A_{hf} and hyperfine fields H_{hf} (experimental and calculated dipolar) are discussed in the text.

Line i	A_i^{TF}	$\omega_i/2\pi$ (MHz)	σ_i (μs^{-1})	A_{hf} (mol/emu)	$H_{\mathrm{hf}}^{\mathrm{(exp)}}$ (kOe/μ_B per Yb)	$H_{\mathrm{hf}}^{\mathrm{(dip)a}}$ (kOe/μ_B per Yb)
1	0.140(7)	140.2(3)	32.5(1.3)	0.23(1)	1.26(6)	-1.174 ($\mu 1$)
2	0.149(5)	136.760(5)	1.47(2)	0.13(1)	0.73(5)	0.897 ($\mu 2$)
3	0.027(5)	136.23(1)	1.04(5)	–	–	–

^{a}From lattice sums of nuclear dipolar fields.

so that $A_{\mathrm{Ld}} = -0.12(2)$ mol emu^{-1}. This correction can be important in μSR shift measurements.

The rates σ_i in Table I are faster than the dynamic rates discussed below in Secs. III B and III C, particularly for line 3. σ_i is therefore attributed to static distributions of TF frequencies, most likely related to the crystalline-electric-field randomness observed in neutron scattering [19], which leads to rms widths $\delta K = \sigma/\omega_3$ of Knight shift distributions. We do not fully understand the large difference between σ_1 and σ_2.

The temperature dependencies of K_{raw}, K_{corr}, and δK for lines 1 and 2 are given in Fig. 3. The error in K_{corr} is largely due to uncertainty in A_{Ld} [Eq. (3)]. Over the temperature range of the data both the Knight shifts and $\chi_{\mathrm{mol}}(T) = M(T)/H$ in 10 kOe [24] are practically constant.

The relation between the Knight shift and χ_{mol} is often analyzed using the Clogston-Jaccarino relation [46]:

$$K_{\mathrm{corr}}(T) = K_0 + A_{\mathrm{hf}}\,\chi_{\mathrm{mol}}(T), \qquad (4)$$
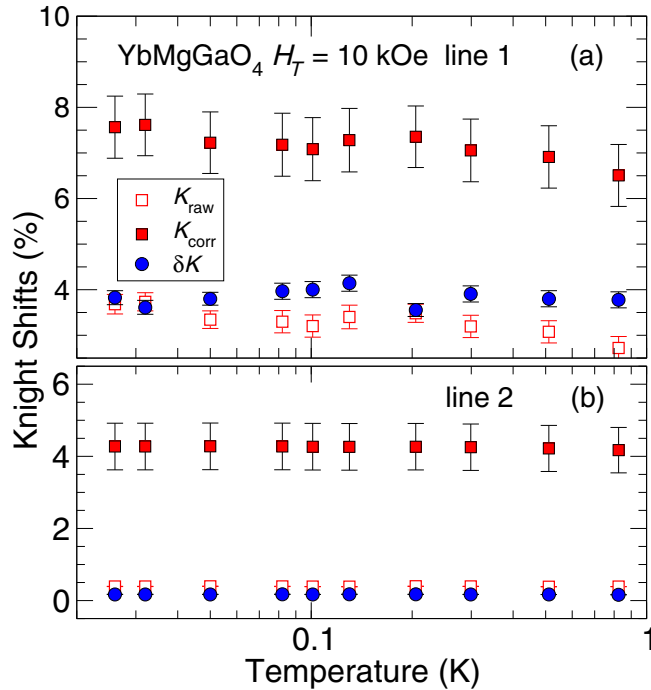

FIG. 3. Temperature dependence of μ^+ Knight shifts in YbMgGaO$_4$ (Fig. 2). (a) Line 1. (b) Line 2. Open squares: raw shifts K_{raw}. Filled squares: corrected shifts K_{corr} (see text). Circles: rms distribution widths $\delta K = \sigma/\omega_3$ (Table I).

where A_{hf} is the hyperfine coupling constant and temperature is an implicit variable. In the present case there is not enough temperature dependence to either quantity for this procedure to be reliable. Instead, we assume K_0 in Eq. (4) is negligible, as would be expected in a magnetic insulator, so that $A_{\mathrm{hf}} = K_{\mathrm{corr}}/\chi_{\mathrm{mol}}$. The hyperfine field H_{hf} (the local field at a μ^+ site per μ_B of paramagnetic moment on the local-moment sites) is given by $H_{\mathrm{hf}} = N_A \mu_B A_{\mathrm{hf}}$, where N_A is Avogadro's number.

Values of A_{hf} and H_{hf} for the two lines are given in Table I. Also included in Table I are calculated Yb^{3+} dipolar hyperfine fields at each of the two candidate μ^+ sites discussed in Sec. II A (Appendix A); local-moment/μ^+ coupling fields are expected to be predominantly dipolar in insulators [32]. The calculated and measured values are of the same order of magnitude but with a discrepancy in sign for line 1. This is not understood, but it may mean that the location of site $\mu 1$ is incorrect.

B. Longitudinal-field μSR

1. $H_L \geqslant 25$ Oe, two-exponential relaxation

We first consider data for H_L strong enough to decouple any nuclear dipolar fields at μ^+ sites. Then the relaxation is purely dynamic and its analysis is simplified.

The observation of two sample lines in TF-μSR and their identification with distinct μ^+ sites motivates fitting the data to a sum of two exponentials,

$$A_d(t) = A_0 \sum_{i=1}^{2} f_i \exp(-\lambda_i t) + A_{\mathrm{Ag}}, \qquad (5)$$

rather than the stretched exponential used previously [15]. Here A_0 is the initial sample asymmetry, λ_1 and λ_2 are the fast and slow relaxation rates, respectively, A_{Ag} is the asymmetry of the background silver signal noted above in Sec. III A, and $f_1 + f_2 = 1$. Good fits to the data (Appendix B) were obtained using Eq. (5), with f_2 fixed at 0.52 from the amplitudes of the TF lines (Table I). This is *a posteriori* justification for the assumption that lines 1 and 2 arise from the sample; the amplitude of line 3 is too small to produce significantly subexponential relaxation.

The field dependencies of the fast rate λ_1 and the ratio λ_2/λ_1 at $T = 22$ mK are shown in Fig. 4 for intermediate fields. For 25 Oe $\lesssim H_L \lesssim 500$ Oe, the ratio $\lambda_2/\lambda_1 = 0.03(1)$ is basically constant and agrees roughly with the value 0.021 from a lattice sum of uncorrelated mean-square Yb^{3+} dipolar fields at the candidate μ^+ sites (Appendix A). This is expected in the fast-fluctuation (motionally narrowed) limit if the
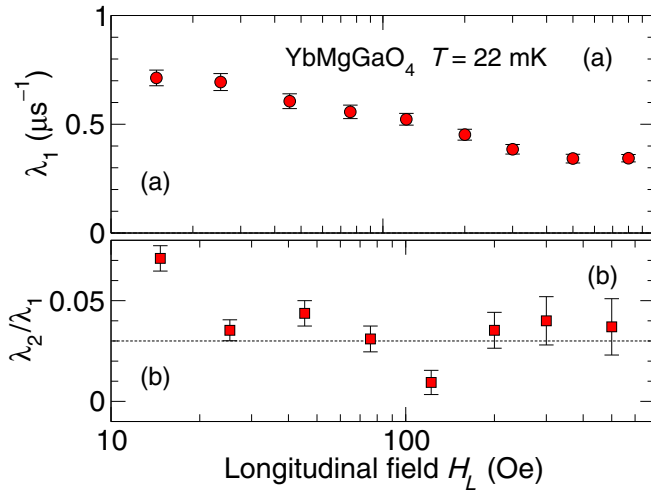
FIG. 4. Field dependencies of dynamical relaxation rates from two-exponential fits to LF-μSR data in YbMgGaO$_4$, $T = 22$ mK. (a) Rapid relaxation rate λ_1. (b) Ratio of rates λ_2/λ_1.

fluctuation rates at the two sites are the same and the correlation length for the fluctuations is short [47].

Its small value makes λ_2 difficult to measure accurately. Furthermore, for $H_L \gtrsim 800$ Oe, λ_1 becomes too slow to permit distinguishing the two components from data in the μSR time window (Appendix B), so that λ_2 cannot be determined at high fields. This together with its observed proportionality to λ_1 (Fig. 4) justifies consideration only of the latter in the following.

The increase of λ_2/λ_1 at 14 Oe (Fig. 4) signals the onset of static relaxation at low fields. As discussed below in Sec. IV, in zero and low fields a static (Gaussian) local-field component reduces the subexponential character of the relaxation, thereby increasing λ_2/λ_1 in the now-incorrect two-exponential fit.

2. $0 \leqslant H_L \lesssim 8$ kOe, two-exponential + KT static relaxation

In the presence of static nuclear dipolar local fields, both static and dynamic processes contribute to μ^+ relaxation at low LF. For the two-site scenario, the asymmetry function becomes

$$A(H_L, t) = A_0 \sum_{i=1}^{2} f_i \exp(-\lambda_i t) G_{\mathrm{KT}}(H_L, \Delta_i, t) + A_{\mathrm{Ag}}, \quad (6)$$

where $G_{\mathrm{KT}}(H_L, \Delta, t)$ is the static KT function for Gaussian local-field distributions [41]. Here Δ/γ_μ is the rms width of the Gaussian field distribution, where $\gamma_\mu/2\pi = 1.3553 \times 10^4$ Hz G^{-1} is the μ^+ gyromagnetic ratio. In YbMgGaO$_4$ we attribute this distribution to nuclear dipolar fields: $\Delta_i = \Delta_i^{\mathrm{nuc}}$.

Equation (6) is also valid for $H_L = 0$, where it is most sensitive to the values of the Δ_i^{nuc}. These were determined by fits of Eq. (6) to ZF data, discussed in more detail in Sec. III C. For fits to the LF data, λ_2/λ_1 and the Δ_i^{nuc} were fixed at 0.03 and their ZF values, respectively.

Figure 5 shows asymmetry spectra for representative values of H_L. At low fields the field dependence is dominated by decoupling of the static relaxation, with its characteristic
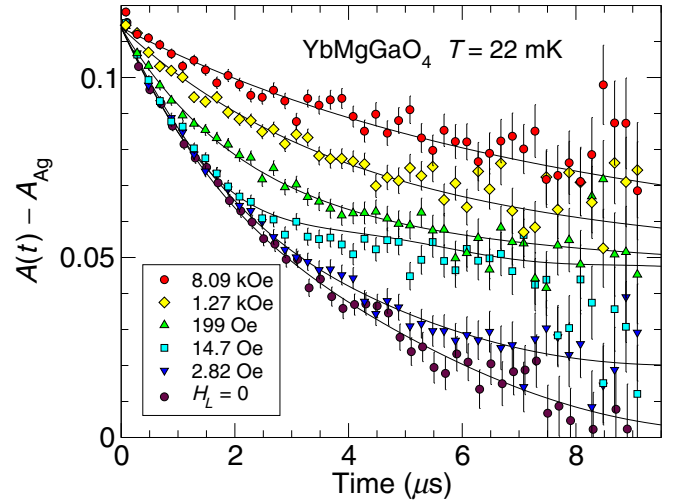
field independence at early times. At higher fields the predominantly dynamic relaxation becomes slower with increasing field as previously reported [15].

The field dependencies of λ_1 at temperatures of 22 mK, 0.20 K, and 5.83 K are shown in Fig. 6, together with stretched-exponential rates λ^* for $T = 70$ mK from Ref. [15]. The λ_1 values for 22 mK are in agreement with the two-exponential fit results for $H_L \gtrsim 45$ Oe, since $G_{\mathrm{KT}}(H_L, \Delta, t) \to 1$ for $H_L \gg \Delta/\gamma_\mu$. $\lambda_1(H_L)$ and $\lambda^*(H_L)$ follow the same trend but do not agree quantitatively because the assumed relaxation functions are different.

The straight line in Fig. 6 is a power-law fit to the 22-mK data for 25 Oe $\leqslant H_L \leqslant 2$ kOe, almost two decades of field values. Power-law behavior is a form of time-field

FIG. 5. LF-μSR asymmetry spectra in YbMgGaO$_4$, $T = 22$ mK, $0 \leqslant H_L \lesssim 8$ kOe, after subtraction of a nonrelaxing signal from the sample holder. Curves: fits of Eq. (6) to the data.
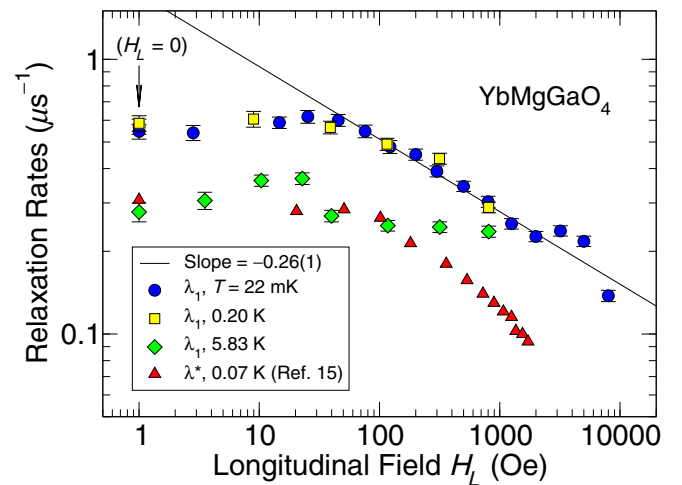

FIG. 6. Field dependencies of dynamic relaxation rates from fits to LF-μSR data in YbMgGaO$_4$, $T = 22$ mK (circles), 0.20 K (squares), and 5.83 K (diamonds). λ_1: fast rate from two-exponential-damped static Gaussian KT fits. λ^*: stretched-exponential rate from Ref. [15], $T = 70$ mK (triangles). Straight line: power-law fit to 22-mK data for 25 Oe $\leqslant H_L \leqslant 2$ kOe.

scaling [48], since $P_\mu(H_L, t) = P_\mu[\lambda_i(H_L)t] = P_\mu(H_L^{-x}t)$ for $\lambda_i \propto H_L^{-x}$. Time-field scaling is in general indicative of long-lived spin correlations with a power-law divergence in the noise spectrum as $\omega \to 0$. This result is consistent with the conclusion of Li *et al.* [15] from a more detailed analysis.

At 5.83 K the rates are reduced and exhibit a plateau for $H_L \gtrsim 40$ Oe. The rather abrupt crossover may be to a normal paramagnetic state, in which local-moment fluctuations are independent of both field and temperature [49].

C. Zero-field μSR

1. ZF asymmetry spectra

Extraction of parameters in Eq. (6) from fits in ZF and weak LF that include static nuclear dipolar relaxation is difficult, because the data are smooth and without distinguishing features (Figs. 5 and 7). Fits with all parameters free lead to excessive scatter, so that it is necessary to fix as many parameters as possible.

Fixing $f_2 = 0.52$ and $\lambda_2/\lambda_1 = 0.03$ have been discussed above. The Δ_i^{nuc} were then allowed to vary, leading to fits (not shown) with excessive scatter but reasonably temperature-independent Δ_i^{nuc} values below $\sim$0.5 K. The data were finally refit with Δ_i^{nuc} fixed at their averages $\Delta_1^{\text{nuc}} = 0.21(2)\,\mu\text{s}^{-1}$ and $\Delta_2^{\text{nuc}} = 0.15(1)\,\mu\text{s}^{-1}$. No temperature dependence of the nuclear dipolar relaxation is expected in the absence of μ^+ diffusion, which is unlikely at low temperatures [32].

ZF-μSR asymmetry spectra for $T = 22$ mK, 0.17 K, and 6.00 K are shown in Fig. 7, again with the silver background signal subtracted. The solid curves are fits of Eq. (6) to the data. The temperature dependence of the overall relaxation over this range is weak because of the temperature-independent static KT contribution, and there is essentially
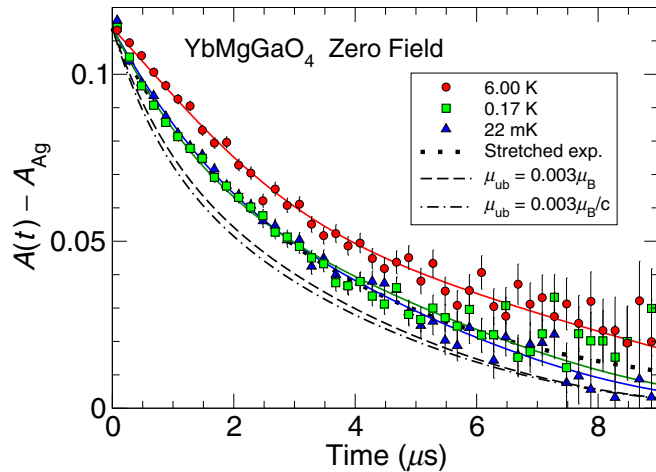

FIG. 7. ZF asymmetry spectra from YbMgGaO$_4$, $T = 22$ mK (triangles), 0.17 K (squares), and 6.00 K (circles), after subtraction of a nonrelaxing signal from the silver sample holder. Solid curves: fits of Eq. (6) to the data. Dotted curve: stretched-exponential fit for 22 mK. Dashed curve: fit spectrum for 22 mK with additional static Gaussian relaxation, moments $0.003\,\mu_B$ per Yb ion. Dash-dot curve: fit spectrum for 22 mK with additional static spin-glass relaxation, moment-concentration product $\mu = 0.003\,\mu_B/c$ per Yb ion (see text).

no temperature dependence between 0.17 K and 22 mK. We observe no oscillating signal due to long-range magnetic order and no initial rapid relaxation or asymmetry loss due to short-range magnetic order [47] down to 22 mK. The dotted curve is a stretched-exponential fit for $T = 22$ mK, illustrating the similarity between it and the two-exponential fit. The dashed and dash-dot curves are discussed in the next section.

2. Limits on static magnetism

To determine upper bounds on static magnetism in YbMgGaO$_4$, two scenarios are considered: equal (small) moments on all Yb^{3+} ions (moment concentration $c = 1$) and the dilute spin-glass limit for small c. For each of these we begin with the ZF data and fit to Eq. (6) for $T = 22$ mK. Upper bounds μ_{ub} on the static moment per Yb ion are chosen, and the corresponding calculated asymmetry spectra are compared with the data. The upper bounds are then adjusted to yield well-resolved increases in relaxation. The results are shown in Fig. 7 for the $c = 1$ and dilute limits by the dashed and dash-dot curves, respectively.

For $c = 1$ the Yb^{3+} dipolar field contribution from disordered Yb^{3+} moments is Gaussian [50], and additional ZF relaxation below a transition temperature increases the values of the Gaussian rates Δ_i in Eq. (6) [51]. Gaussian rms field widths $(\Delta_i^{(0)}/\gamma_\mu)/\mu_B$ per Yb ion were calculated from dipole-field lattice sums (Appendix A) at the candidate μ^+ sites μ1 and μ2 of Fig. 1, yielding $\Delta_1^{(0)} = 147\,\mu\text{s}^{-1}/\mu_B$ and $\Delta_2^{(0)} = 46\,\mu\text{s}^{-1}/\mu_B$.

An upper bound μ_{ub} on the static moment per Yb ion is found by comparing Eq. (6) with increased rates $\Delta_i' = [(\Delta_i^{\text{nuc}})^2 + (\mu_{\text{ub}}\Delta_i^{(0)})^2]^{1/2}$ to the data. The choice $\mu_{\text{ub}} = 0.003\,\mu_B$ per Yb ion results in the dashed curve in Fig. 7, which exhibits a well-resolved increase. For comparison, dc susceptibility measurements in YbMgGa)$_4$ [23,24], which, like μSR, probe the bulk magnetization, yield paramagnetic Curie-Weiss and saturated moments $\sim$3 μ_B per Yb ion.

We next consider dilute (disordered) static Yb^{3+} moments. The Lorentzian ZF KT relaxation function [50]

$$G_{\text{KT}}^{\text{Lor}}(a.t) = \tfrac{2}{3} + \tfrac{1}{3}(1 - at)\exp(-at) \qquad (7)$$

is expected from dipolar coupling to a static random spin system in the dilute limit. Here a/γ_μ is the half-width of the Lorentzian dipolar field distribution [50],

$$a = (\pi/2)^{1/2}c\mu\Delta^{(0)}, \qquad (8)$$

where μ is the moment per (dilute) Yb ion per Bohr magneton. The resulting relaxation function is derived from Eq. (6) by multiplying each term by $G_{\text{KT}}^{\text{Lor}}(a_i, t)$. We choose a value $\mu_{\text{ub}} = 0.003/c$ (e.g., for concentration $c = 0.01$ $\mu_{\text{ub}} = 0.3\mu_B$ per Yb ion) and determine the a_i from Eq. (8), resulting in the dash-dot curve in Fig. 7. Again, the increase is well resolved.

Somewhat surprisingly, the sample-average $c = 1$ and dilute bounds are identical. The results cannot be taken as quantitative, however, since they involve the assumed μ^+ sites and do not employ a well-defined resolution criterion. They are solely intended to demonstrate the basic sensitivity of the μSR technique to weak static magnetism.
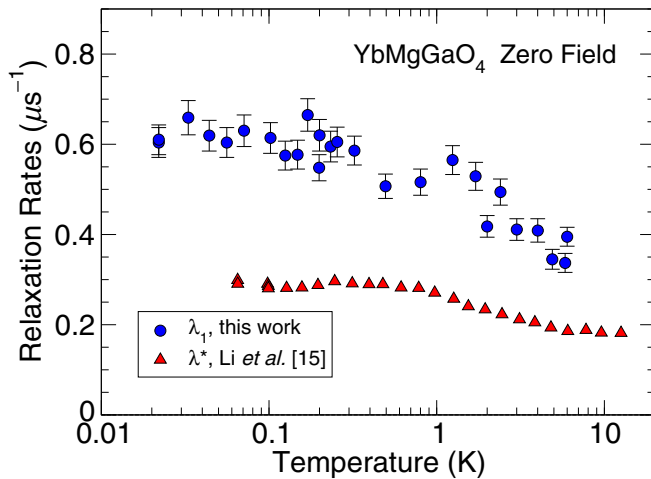
FIG. 8. Temperature dependencies of ZF μ^+ relaxation rates in YbMgGaO$_4$ from fits of Eq. (6) to the data. Circles: this work, from fits of Eq. (6) to the data. Triangles: results of Li *et al.* [15].

3. Temperature dependence of zero-field rates

Figure 8 shows the temperature dependence of the ZF dynamic relaxation rate $\lambda_1(T)$ (circles) from fits of Eq. (6) to the data discussed above and also gives $\lambda^*(T)$ from Li *et al.* [15] (triangles). With decreasing temperature, the rates increase and saturate below $\sim$0.4 K, exhibiting persistent spin dynamics down to the lowest temperatures. The scatter in $\lambda_1(T)$ is mainly due to the fact that in ZF the dynamic relaxation is only a fraction of the total relaxation.

The difference between $\lambda_1(T)$ and $\lambda^*(T)$ is again a consequence of the different assumed relaxation functions. Furthermore, as noted above, in ZF and weak LF "pure" stretched-exponential fits [i.e., without the factor $G_{KT}(H_L, \Delta, t)$ of Eq. (6)] mix the static and dynamic contributions.

IV. DISCUSSION

Our μSR study extends previous results [15] concerning the nature of the ground state and low-lying excitations in YbMgGaO$_4$. The observation of the same field dependence $\lambda_1(H_L)$ at 22 mK and 0.20 K for fields up to 0.8 kOe (Fig. 6) complements the previously reported temperature independence of ZF μ^+ relaxation below $\sim$0.4 K [15] and is strong evidence that the system is in a temperature-independent state over this region in the *H-T* phase diagram.

A. Limits on spin freezing

μSR experiments are extremely sensitive to static magnetism, ordered or disordered [32], in the present case with an upper limit $\sim 10^{-3} \mu_B$ per Yb ion on any sample-average static Yb^{3+} moment down to 22 mK (Sec. III C 2). This is a strong constraint on proposals involving magnetic ground states [28–31], although in the disordered local-singlet valence solid [31] the "ultimate fate of the ...defect spins is unknown."

The lack of spin freezing is in apparent contradiction with the observation of a cusp in the low-field ac susceptibility of YbMgGaO$_4$ at $\sim$0.1 K [23] and the conclusion that a spin-glass-like transition occurs there. We note that suppression

of static order by the muon itself, a possible explanation of this discrepancy, has been shown to be unlikely [52]. We also note that large static Yb^{3+} moments in a macroscopic spurious phase would result in a fraction of the ZF asymmetry spectrum with oscillations or rapid relaxation. This is not seen at the level of a few percent. The resolution of these issues is not clear, and more work will be required to elucidate the impact of the present results on the QSL debate.

B. Characterization of sample inhomogeneity, consequences for ZF results

Our μSR results suggest reinterpretation of some of the previous work. The observation of two equal-amplitude lines in the TF-μSR data is evidence for the two μ^+ stopping sites in the two inequivalent O^{2-} lattice planes. This, rather than, for example, Mg^{2+}/Ga^{3+} site mixing [19], is the main source of inhomogeneity in the dynamic relaxation and strongly suggests a two-exponential analysis of LF- and ZF-μSR data [Eqs. (5) and (6)] rather than a stretched-exponential analysis.

The fact that good fits can be obtained with either two-exponential or stretched-exponential functions is not surprising. In general, the relaxation function $P(t)$ associated with a spatially inhomogeneous distribution $P(\lambda)$ of rates λ is given by the Laplace transform

$$P(t) = \int_{-\infty}^{\infty} P(\lambda) \exp(-\lambda t)\, d\lambda. \qquad (9)$$

Two-exponential and stretched-exponential functions are effectively two choices of $P(\lambda)$.

Solving Eq. (9) for $P(\lambda)$ is a mathematically ill-posed problem [53]; $P(t)$ is not sensitive to the form of $P(\lambda)$. The difficulty is greater when the range of the independent variable is limited, as it is for μSR asymmetry spectra by the muon lifetime [54]. We also note that for $P(t) = \exp[-(\lambda^* t)^\beta]$, the relation of λ^* to $P(\lambda)$ depends on β; λ^* is not simply an average rate, and one should not compare values of λ^* for different values of β [38].

The temperature dependence of β in fits to ZF data is also consistent with the two-exponential scenario. (Quasi)static relaxation in ZF and weak LF by nuclear dipolar fields should not be ignored, although the lack of structure in the μ^+ asymmetry spectra and the limitation imposed by the muon lifetime make the analysis difficult. We argue that the reported increase of β with increasing temperature in ZF stretched-exponential fits is not a temperature-dependent effect of the spin dynamics [15]. Instead, the decrease of ZF dynamic relaxation with increasing temperature (Fig. 8) increases the importance of the temperature-independent "super-exponential" (Gaussian) nuclear dipolar field distribution. This renders the overall ZF relaxation function less subexponential at high temperatures, leading to $\beta \approx 1$ at $\sim$10 K [15].

V. CONCLUSIONS

We have carried out μSR experiments on single-crystalline samples of the candidate spin-liquid YbMgGaO$_4$, which complement and extend earlier work [15]. The spatial inhomogeneity that gives rise to subexponential μ^+ spin relaxation is attributed to two distinct μ^+ stopping sites in the unit cell,

rather than Mg^{2+}/Ga^{3+} site mixing or other local disorder. With an upper bound of $\sim 3 \times 10^{-3} \mu_B$/Yb ion, no static magnetism, ordered or disordered, is observed down to 22 mK, a factor of 2 lower in temperature than previous measurements. The field dependence of the μ^+ spin relaxation is the same in functional form and relaxation rate at 22 mK and 0.20 K up to at least 1 kOe. These results indicate persistent (i.e., temperature-independent) spin dynamics with no spin freezing for this field and temperature range, thus extending the previous ZF results [15] over a substantial region of the *H*-*T* phase diagram.

ACKNOWLEDGMENTS

APPENDIX A: DIPOLAR LATTICE SUMS

The dipolar lattice-sum calculation is straightforward. The software sets up a general orthorhombic lattice (with a nonprimitive unit cell for a triangular structure such as that of YbMgGaO$_4$). 1-μ_B local moments are placed at lattice sites in the magnetic structure (with or without a net moment in the unit cell), and candidate μ^+ stopping sites in the unit cell are designated. For each μ^+ site, dipolar fields from the local moments are summed between an inner cutoff radius (if desired) and an outer Lorentz sphere radius R_{Lor}. The value of R_{Lor} is chosen so that larger values have a negligible effect; typically $R_{\text{Lor}} = 200$ Å, containing 10^5–10^6 moments, is sufficient. For a paramagnet the moments are all in the same direction, induced by the applied field, and the shift is given by the resultant field in that direction. Mean-square fields, which are involved in fluctuation-induced dynamic relaxation,
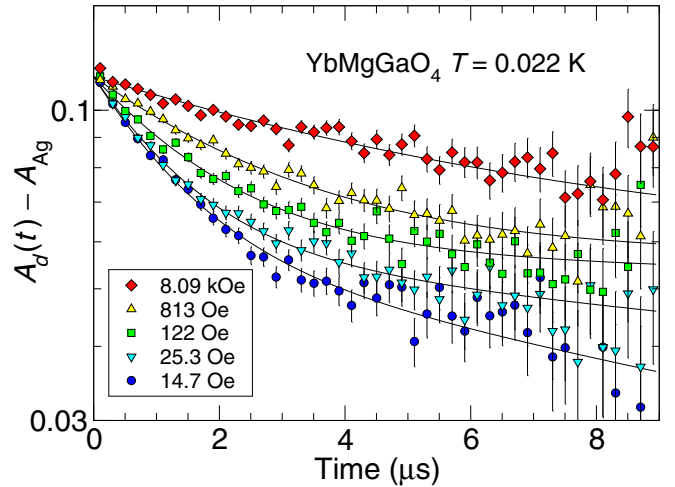

FIG. 9. Log-linear plots of LF asymmetry spectra from YbMgGaO$_4$, $T = 22$ mK, after subtraction of a nonrelaxing signal from the silver sample holder. Curves: fits of Eq. (5) to the data. The visibly faster slow-component relaxation at 14.7 Oe is attributed to static nuclear dipolar fields.

are calculated by summing the squared magnitudes of the individual moment fields. The calculated fields are in units of [field] per μ_B local moment. No Lorentz or demagnetizing corrections are made.

APPENDIX B: TWO-EXPONENTIAL FITS

Figure 9 shows log-linear plots of representative LF asymmetry spectra at 22 mK, 14.7 Oe $\leqslant H_L \leqslant$ 8.09 kOe. Upward curvature is clearly visible. The curves are two-exponential fits to Eq. (5) with the slowly relaxing fraction f_2 fixed at 0.52 (see main text). The fits are good at all fields, but for $H_L = 14.7$ Oe the upward curvature is reduced. As discussed in Secs. III B 1 and IV, this is expected at low enough LF to permit static relaxation by nuclear dipolar fields. For $H_L \gtrsim 1$ kOe, the overall relaxation has slowed enough so that the late-time slow exponential is no longer visible in the experimental time window.

[1] P. W. Anderson, Resonating valence bonds: A new kind of insulator? Mater. Res. Bull. **8**, 153 (1973).

[2] P. W. Anderson, The resonating valence bond state in La$_2$CuO$_4$ and superconductivity, Science **235**, 1196 (1987).

[3] P. A. Lee, An end to the drought of quantum spin liquids, Science **321**, 1306 (2008).

[4] L. Balents, Spin liquids in frustrated magnets, Nature (London) **464**, 199 (2010).

[5] L. Savary and L. Balents, Quantum spin liquids: A review, Rep. Prog. Phys. **80**, 016502 (2017).

[6] Y. Zhou, K. Kanoda, and T.-K. Ng, Quantum spin liquid states, Rev. Mod. Phys. **89**, 025003 (2017).

[7] Y. J. Uemura, A. Keren, K. Kojima, L. P. Le, G. M. Luke, W. D. Wu, Y. Ajiro, T. Asano, Y. Kuriyama, M. Mekata, H. Kikuchi,

and K. Kakurai, Spin Fluctuations in Frustrated Kagomé Lattice System SrCr$_8$Ga$_4$O$_{19}$ Studied by Muon Spin Relaxation, Phys. Rev. Lett. **73**, 3306 (1994).

[8] Y. Shimizu, K. Miyagawa, K. Kanoda, M. Maesato, and G. Saito, Spin Liquid State in an Organic Mott Insulator with a Triangular Lattice, Phys. Rev. Lett. **91**, 107001 (2003).

[9] S. Nakatsuji, Y. Machida, Y. Maeno, T. Tayama, T. Sakakibara, J. van Duijn, L. Balicas, J. N. Millican, R. T. Macaluso, and J. Y. Chan, Metallic Spin-Liquid Behavior of the Geometrically Frustrated Kondo Lattice Pr$_2$Ir$_2$O$_7$, Phys. Rev. Lett. **96**, 087204 (2006).

[10] J. S. Helton, K. Matan, M. P. Shores, E. A. Nytko, B. M. Bartlett, Y. Yoshida, Y. Takano, A. Suslov, Y. Qiu, J.-H. Chung, D. G. Nocera, and Y. S. Lee, Spin Dynamics of the Spin-1/2

Kagome Lattice Antiferromagnet $ZnCu_3(OH)_6Cl_2$, Phys. Rev. Lett. **98**, 107204 (2007).

[11] Y. Okamoto, M. Nohara, H. Aruga-Katori, and H. Takagi, Spin-Liquid State in the $S = 1/2$ Hyperkagome Antiferromagnet $Na_4Ir_3O_8$, Phys. Rev. Lett. **99**, 137207 (2007).

[12] T. Itou, A. Oyamada, S. Maegawa, M. Tamura, and R. Kato, Quantum spin liquid in the spin-1/2 triangular antiferromagnet $EtMe_3Sb[Pd(dmit)_2]_2$, Phys. Rev. B **77**, 104413 (2008).

[13] Y. Li, H. Liao, Z. Zhang, S. Li, F. Jin, L. Ling, L. Zhang, Y. Zou, L. Pi, Z. Yang, J. Wang, Z. Wu, and Q. Zhang, Gapless quantum spin liquid ground state in the two-dimensional spin-1/2 triangular antiferromagnet $YbMgGaO_4$, Sci. Rep. **5**, 16419 (2015).

[14] Y. Li, G. Chen, W. Tong, L. Pi, J. Liu, Z. Yang, X. Wang, and Q. Zhang, Rare-Earth Triangular Lattice Spin Liquid: A Single-Crystal Study of $YbMgGaO_4$, Phys. Rev. Lett. **115**, 167203 (2015).

[15] Y. Li, D. Adroja, P. K. Biswas, P. J. Baker, Q. Zhang, J. Liu, A. A. Tsirlin, P. Gegenwart, and Q. Zhang, Muon Spin Relaxation Evidence for the U(1) Quantum Spin-Liquid Ground State in the Triangular Antiferromagnet $YbMgGaO_4$, Phys. Rev. Lett. **117**, 097201 (2016).

[16] Y. Xu, J. Zhang, Y. S. Li, Y. J. Yu, X. C. Hong, Q. M. Zhang, and S. Y. Li, Absence of Magnetic Thermal Conductivity in the Quantum Spin-Liquid Candidate $YbMgGaO_4$, Phys. Rev. Lett. **117**, 267202 (2016).

[17] Y. Shen, Y.-D. Li, H. Wo, Y. Li, S. Shen, B. Pan, Q. Wang, H. C. Walker, P. Steffens, M. Boehm, Y. Hao, D. L. Quintero-Castro, L. W. Harriger, M. D. Frontzek, L. Hao, S. Meng, Q. Zhang, G. Chen, and J. Zhao, Evidence for a spinon Fermi surface in a triangular-lattice quantum-spin-liquid candidate, Nature (London) **540**, 559 (2016).

[18] J. A. M. Paddison, M. Daum, Z. Dun, G. Ehlers, Y. Liu, M. B. Stone, H. Zhou, and M. Mourigal, Continuous excitations of the triangular-lattice quantum spin liquid $YbMgGaO_4$, Nat. Phys. **13**, 117 (2017).

[19] Y. Li, D. Adroja, R. I. Bewley, D. Voneshen, A. A. Tsirlin, P. Gegenwart, and Q. Zhang, Crystalline Electric-Field Randomness in the Triangular Lattice Spin-Liquid $YbMgGaO_4$, Phys. Rev. Lett. **118**, 107202 (2017).

[20] Y. Li, D. Adroja, D. Voneshen, R. I. Bewley, Q. Zhang, A. A. Tsirlin, and P. Gegenwart, Nearest-neighbour resonating valence bonds in $YbMgGaO_4$, Nat. Commun. **8**, 15814 (2017).

[21] Y. Shen, Y. Li, H. Walker, P. Steffens, M. Boehm, X. Zhang, S. Shen, H. Wo, G. Chen, and J. Zhao, Fractionalized excitations in the partially magnetized spin liquid candidate $YbMgGaO_4$, Nat. Commun. **9**, 4138 (2018).

[22] X. Zhang, F. Mahmood, M. Daum, Z. Dun, J. A. M. Paddison, N. J. Laurita, T. Hong, H. Zhou, N. P. Armitage, and M. Mourigal, Hierarchy of Exchange Interactions in the Triangular-Lattice Spin Liquid $YbMgGaO_4$, Phys. Rev. X **8**, 031001 (2018).

[23] Z. Ma, J. Wang, Z.-Y. Dong, J. Zhang, S. Li, S.-H. Zheng, Y. Yu, W. Wang, L. Che, K. Ran, S. Bao, Z. Cai, P. Čermák, A. Schneidewind, S. Yano, J. S. Gardner, X. Lu, S.-L. Yu, J.-M. Liu, S. Li, J.-X. Li, and J. Wen, Spin-Glass Ground State in a Triangular-Lattice Compound $YbZnGaO_4$, Phys. Rev. Lett. **120**, 087201 (2018).

[24] Y. Li, S. Bachus, B. Liu, I. Radelytskyi, A. Bertin, A. Schneidewind, Y. Tokiwa, A. A. Tsirlin, and P. Gegenwart,

Rearrangement of Uncorrelated Valence Bonds Evidenced by Low-Energy Spin Excitations in $YbMgGaO_4$, Phys. Rev. Lett. **122**, 137201 (2019).

[25] Y.-D. Li, X. Wang, and G. Chen, Anisotropic spin model of strong spin-orbit-coupled triangular antiferromagnets, Phys. Rev. B **94**, 035107 (2016).

[26] Y.-D. Li, Y.-M. Lu, and G. Chen, Spinon Fermi surface $U(1)$ spin liquid in the spin-orbit-coupled triangular-lattice Mott insulator $YbMgGaO_4$, Phys. Rev. B **96**, 054445 (2017).

[27] Y.-D. Li and G. Chen, Detecting spin fractionalization in a spinon Fermi surface spin liquid, Phys. Rev. B **96**, 075105 (2017).

[28] Q. Luo, S. Hu, B. Xi, J. Zhao, and X. Wang, Ground-state phase diagram of an anisotropic spin-$\frac{1}{2}$ model on the triangular lattice, Phys. Rev. B **95**, 165110 (2017).

[29] Z. Zhu, P. A. Maksimov, S. R. White, and A. L. Chernyshev, Disorder-Induced Mimicry of a Spin Liquid in $YbMgGaO_4$, Phys. Rev. Lett. **119**, 157201 (2017).

[30] E. Parker and L. Balents, Finite-temperature behavior of a classical spin-orbit-coupled model for $YbMgGaO_4$ with and without bond disorder, Phys. Rev. B **97**, 184413 (2018).

[31] I. Kimchi, A. Nahum, and T. Senthil, Valence Bonds in Random Quantum Magnets: Theory and Application to $YbMgGaO_4$, Phys. Rev. X **8**, 031028 (2018).

[32] A. Schenck, Muon Spin Rotation Spectroscopy: Principles and Applications in Solid State Physics (A. Hilger, Bristol & Boston, 1985) S. J. Blundell, Spin-polarized muons in condensed matter physics, Contemp. Phys. **40**, 175 (1999); J. H. Brewer, in *Digital Encyclopedia of Applied Physics*, edited by G. L. Trigg, E. S. Vera, and W. Greulich (Wiley-VCH Verlag GmbH & Co KGaA, Weinheim, 2003); A. Yaouanc and P. Dalmas de Réotier, *Muon Spin Rotation, Relaxation, and Resonance: Applications to Condensed Matter*, International Series of Monographs on Physics (Oxford University Press, New York, 2011).

[33] F. Bert, A. Olariu, A. Zorko, P. Mendels, J. C. Trombe, F. Duc, M. A. d. Vries, A. Harrison, A. D. Hillier, J. Lord, A. Amato, and C. Baines, Frustrated magnetism in the quantum Kagome Herbertsmithite $ZnCu_3(OH)_6Cl_2$ antiferromagnet, J. Phys. Conf. Ser. **145**, 012004 (2009).

[34] F. L. Pratt, P. J. Baker, S. J. Blundell, T. Lancaster, S. Ohira-Kawamura, C. Baines, Y. Shimizu, K. Kanoda, I. Watanabe, and G. Saito, Magnetic and non-magnetic phases of a quantum spin liquid, Nature (London) **471**, 612 (2011).

[35] L. Clark, J. C. Orain, F. Bert, M. A. De Vries, F. H. Aidoudi, R. E. Morris, P. Lightfoot, J. S. Lord, M. T. F. Telling, P. Bonville, J. P. Attfield, P. Mendels, and A. Harrison, Gapless Spin Liquid Ground State in the $S=1/2$ Vanadium Oxyfluoride Kagome Antiferromagnet $[NH_4]_2[C_7H_{14}N][V_7O_6F_{18}]$, Phys. Rev. Lett. **110**, 207208 (2013).

[36] P. Khuntia, F. Bert, P. Mendels, B. Koteswararao, A. V. Mahajan, M. Baenitz, F. C. Chou, C. Baines, A. Amato, and Y. Furukawa, Spin Liquid State in the 3D Frustrated Antiferromagnet $PbCuTe_2O_6$: NMR and Muon Spin Relaxation Studies, Phys. Rev. Lett. **116**, 107203 (2016).

[37] F. L. Pratt, Probing Quantum Critical Spin Liquids with μSR, JPSJ Conf. Proc. 21, 011002 (2018), Proceedings of the 14th International Conference on Muon Spin Rotation, Relaxation and Resonance (μSR2017).

[38] D. C. Johnston, Stretched exponential relaxation arising from a continuous sum of exponential decays, Phys. Rev. B **74**, 184430 (2006).

[39] P. Bonfà and R. De Renzi, Toward the computational prediction of muon sites and interaction parameters, J. Phys. Soc. Jpn. **85**, 091014 (2016).

[40] W. D. Knight, Nuclear magnetic resonance shift in metals, Phys. Rev. **76**, 1259 (1949).

[41] R. S. Hayano, Y. J. Uemura, J. Imazato, N. Nishida, T. Yamazaki, and R. Kubo, Zero- and low-field spin relaxation studied by positive muons, Phys. Rev. B **20**, 850 (1979).

[42] G. D. Morris and R. H. Heffner, A method of achieving accurate zero-field conditions using muonium, Physica B **326**, 252 (2003).

[43] A. Suter and B. Wojek, Musrfit: A free platform-independent framework for μSR data analysis, Phys. Procedia **30**, 69 (2012), 12th International Conference on Muon Spin Rotation, Relaxation and Resonance (μ SR2011).

[44] http://computing.triumf.ca/legacy/physica/.

[45] G. C. Carter, L. H. Bennett, and D. J. Kahan, Metallic shifts in NMR, in *Progress in Materials Science* (Pergamon Press, Oxford & New York, 1977), Vol. 20, pp. 58–59; P. Akishin and I. Gaganov, The macroscopic demagnetizing effects in cylindrical and rectangular box samples, J. Magn. Magn. Mater. **110**, 175 (1992).

[46] A. M. Clogston and V. Jaccarino, Susceptibilities and negative Knight shifts of intermetallic compounds, Phys. Rev. **121**, 1357 (1961).

[47] X. F. Miao, L. Caron, J. Cedervall, P. C. M. Gubbens, P. Dalmas de Réotier, A. Yaouanc, F. Qian, A. R. Wildes, H. Luetkens, A. Amato, N. H. van Dijk, and E. Brück, Short-range magnetic correlations and spin dynamics in the paramagnetic regime of (Mn, Fe)$_2$(P, Si), Phys. Rev. B **94**, 014426 (2016).

[48] A. Keren and G. Bazalitsky, Muon polarization in the presence of exotic spin correlations, Physica B **289-290**, 205 (2000).

[49] T. Moriya, Nuclear magnetic relaxation in antiferromagnetics, Progr. Theoret. Phys. (Kyoto) **16**, 23 (1956).

[50] Y. J. Uemura, T. Yamazaki, D. R. Harshman, M. Senba, and E. J. Ansaldo, Muon-spin relaxation in AuFe and CuMn spin glasses, Phys. Rev. B **31**, 546 (1985).

[51] Long-range magnetic order gives rise to oscillation, which for low frequency varies quadratically with time and cannot be distinguished from a slow Gaussian. The disordered estimate therefore also applies to this case.

[52] A. Keren, Muons as probes of dynamical spin fluctuations: Some new aspects, J. Phys.: Condens. Matter **16**, S4603 (2004).

[53] W. H. Press, S. A. Teukolsky, W. T. Vetterling, and B. P. Flannery, *Numerical Recipes in C*, 2nd ed. (Cambridge University Press, Cambridge, New York, 1992), Chap. 18.

[54] This is the problem in the present case. At late enough times, the sum of two exponentials with very different rates differs significantly from a stretched exponential.